RMetS

Royal Meteorological Society

A study of the air–sea interaction in the South Atlantic Convergence Zone through Granger causality

Giulio Tirabassi,[a]* Cristina Masoller[a] and Marcelo Barreiro[b]

[a] *Universitat Politecnica de Catalunya, Terrassa, Spain*
[b] *Departamento de Ciencias de la Atmosfera, Instituto de Fisica, Universidad de la Republica, Montevideo, Uruguay*

ABSTRACT: Air–sea interaction in the region of the South Atlantic Convergence Zone (SACZ) is studied using Granger causality (GC) as a measure of directional coupling. Calculation of the area weighted connectivity indicates that the SACZ region is the one with largest mutual air–sea connectivity in the south Atlantic basin during summertime. Focusing on the leading mode of daily coupled variability, GC allows distinguishing four regimes characterized by different coupling: there are years in which the forcing is mainly directed from the atmosphere to the ocean, years in which the ocean forces the atmosphere, years in which the influence is mutual and years in which the coupling is not significant. A composite analysis shows that ocean-driven events have atmospheric anomalies that develop first and are strongest over the ocean, while in events without coupling anomalies develop from the continent where they are strongest and have smaller oceanic extension.

1. Introduction

The South Atlantic Convergence Zone (SACZ) is one of the main components of the South American Monsoon: it is a convective pattern that extends from the Amazon forest to the subtropical South Atlantic Ocean (SAO), oriented in northwest–southeast direction (Carvalho *et al.*, 2002, 2004; Bombardi *et al.*, 2013). When active, the SACZ is associated with heavy precipitation over the Amazon forest and southeastern Brazil, causing floods and landslides over the densely populated areas of Minas Gerais, Sao Paulo and Rio de Janeiro.

The main mode of SACZ variability consists of a precipitation dipole with centres over the SACZ and over Uruguay, such that when the SACZ is active there is decreased rainfall over Uruguay and vice versa. This mode varies on several time scales ranging from day-to-day, due to the passage of fronts, to intraseasonal, interannual and even longer time scales having been associated with the observed summertime rainfall trend in eastern South America during the 20th century (Kodama, 1992; Nogués-Paegle and Mo, 1997; Barreiro *et al.*, 2002; Junquas *et al.*, 2012).

Due to its socio-economic importance, there have been several attempts to improve our understanding and predictability of rainfall over the SACZ on seasonal to interannual time scales, particularly focusing on the role of upper ocean in modulating its behaviour. Studies have shown that the subtropical SAO may influence the evolution of

the SACZ (Robertson and Mechoso, 2000; Barreiro *et al.*, 2002, 2005). For example, Barreiro *et al.* (2002, 2005) show that even though the region is dominated by internal atmospheric variability, sea surface temperature (SST) anomalies can force a dipole of precipitation anomalies located mainly over the oceanic portion of the SACZ. Subsequent studies have suggested that the air–sea interaction is such that an initially stronger SACZ – due to internal atmospheric variability – induces an oceanic cooling that in turn negatively affects the convective precipitation, resulting in a negative feedback loop (Chaves and Nobre, 2004; De Almeida *et al.*, 2007).

However, air–sea interaction has been difficult to quantify both in observations and in model simulations and to date it is unclear how the circulation associated with the SACZ is influenced by surface ocean conditions. Disentangling air–sea interaction in the subtropics is a challenging task, and up to now to the best of our knowledge, no method has allowed a robust identification of this interaction in observational data. To tackle this problem, we propose a new methodology based on the combined use of Granger causality (GC) together with a new measure from climate network theory (area weighted connectivity, AWC) and maximum covariance analysis (MCA); this methodology aims to assess the presence of air–sea interaction, and to distinguish among different interaction regimes.

We find that for the leading SACZ mode of variability the air–sea coupling is significantly active only in 50% of the cases, and that when active, it manifests itself in three distinct 'flavours': there are years in which the forcing is mainly directed from the atmosphere to the ocean, years

* Correspondence to: G. Tirabassi, Universitat Politecnica de Catalunya, Terrassa, Spain. E-mail: giulio.tirabassi@upc.edu

in which the ocean forces the atmosphere and years in which the influence is mutual. Moreover, we find that the conditions in the upper ocean can modulate rainfall events in the SACZ, affecting the position, the intensity and the persistence of the precipitation anomalies.

2. Data

As a proxy for precipitation, we consider the vertical velocity at 500 hPa, ω, while the ocean state is characterized by the SST. Both data sets are daily mean data provided by ERA INTERIM reanalysis (Dee *et al.*, 2011), ranging from December 1979 to March 2013 on a horizontal grid with 1.5 degrees of resolution. We restricted the analysis to austral summer months (December–March) when the SACZ shows strongest activity. Anomalies were calculated first removing the annual cycle by subtracting the average value for each day, and then normalizing the series to have unit variance.

3. The GC estimator

We assume that the time series at each grid point can be described by a D-dimensional autoregressive process in the form (Mosedale *et al.*, 2006)

$$Y_t = \sum_{k=1}^{D} a_k Y_{t-k} + \sum_{k=1}^{D} b_k X_{t-k} + \varepsilon_t \qquad (1)$$

where X is the forcing and Y the slave variable. Here a_k and b_k are vectors of coefficients and ε are the associated residuals. Y is either SST or vertical velocity (ω) at a certain location (but not necessarily the same): if $Y = \mathrm{SST}$, then $X = \omega$ and vice versa. Considering two time series at different locations allows analysing non-local air–ocean interactions.

We apply to this autoregressive model a GC test: the first step of this procedure is to fit a_k and b_k with a linear regression, and compute the associated variance of the residuals, $\sigma^2_{\mathrm{coupled}}$. In the second step, the fit is repeated setting $b_k = 0$, and again the variance of the residuals is computed, namely $\sigma^2_{\mathrm{uncoupled}}$. The last step involves comparing the two residual variances: if the variance in the coupled case is smaller than the one computed in the uncoupled one, it means that the predictive power of the coupled model is higher, and thus, X is Granger causal of Y. In other words, X is Granger causal of Y if X helps predict Y at some time in the future. Then, the prediction improvement is measured by the Granger causality estimator (GCE) as in Mokhov *et al.* (2011).

$$\mathrm{GCE} = \frac{\sigma^2_{\mathrm{uncoupled}} - \sigma^2_{\mathrm{coupled}}}{\sigma^2_{\mathrm{uncoupled}}} \qquad (2)$$

We tested the significance of the GCE value with a F-test. X is considered a true Granger causal of Y only if the associated GCE value is significant at a certain confidence level (as explained below, we used 99% confidence level

and 90%, depending on the available statistics). If X is Granger causal of Y, we will denote this fact as $X \rightarrow Y$. If also Y is Granger causal of X, thus forming a closed-loop system, the notation $X \leftrightarrow Y$ will be used instead.

Finally, the dimension of the autoregressive model D, for every time series Y of length T days, is chosen in order to minimize the function,

$$S(D) = \frac{T}{2} \ln\left(\frac{\sigma^2_{\mathrm{uncoupled}}}{\sigma^2_Y}\right) + \frac{D}{2} \ln(T) \qquad (3)$$

that is a good compromise between obtaining a good fitting and avoiding over-fitting (Schwarz, 1978). Typical values of D are about 8 days for SST and 4 days for ω, depending on the location.

GC is a powerful tool for the analysis of climate time series (Stern and Kaufmann, 1999, 2014; Salvucci *et al.*, 2002; Khokhlov *et al.*, 2006; Mosedale *et al.*, 2006; Mokhov *et al.*, 2011; Attanasio *et al.*, 2012; Pasini *et al.*, 2012). It is especially useful in systems that exhibit feedback and closed loops, for which the lagged correlation can lead to misleading conclusions (Chatfield, 1989; Runge *et al.*, 2014). Note, however, that this methodology can detect linear dependencies only and assumes that the time series are covariance stationary. A drawback of the methodology is that if X and Y are strongly influenced by a third unknown factor, the method could find that X is Granger causal of Y even though the real causality is different. Throughout this work, we will consider that X forces Y if X is Granger causal of Y, bearing in mind the previous drawback.

4. Air–sea connectivity

We start by focusing on the region [20N, 40S] × [70W, 20E], and compute the GCE at each grid node, both in the direction SST → ω and ω → SST. In this way, we want to estimate the local interaction between the two systems, i.e. the interaction between a grid point in the ocean and the one placed in the atmosphere just above it. The GCE values at 99% confidence level are plotted in Figure 1. As it can be observed in (a), the main two zones in which the ocean forces the atmosphere are the deep tropics and the subtropical waters off Brazil. The deep tropics is expected to be a region of oceanic forcing (e.g. Hoskins and Karoly, 1981), and the methodology consistently captures this fact. The ocean off southeast Brazil corresponds to the SACZ region and is within our region of interest. Moreover, Figure 1(b) clearly shows that the atmosphere strongly forces the surface ocean also off Brazil. Thus, this ocean region can play both an active and a passive role, providing a hint of the presence of complex feedback loops in the area (Chaves and Nobre, 2004; De Almeida *et al.*, 2007).

As the atmosphere and the ocean interact on larger spatial scales – not only locally – the calculation of the local GCE value provides limited information. Therefore, we computed the cross-GCE, in which the GCE is evaluated, in the two directions, for every couple of
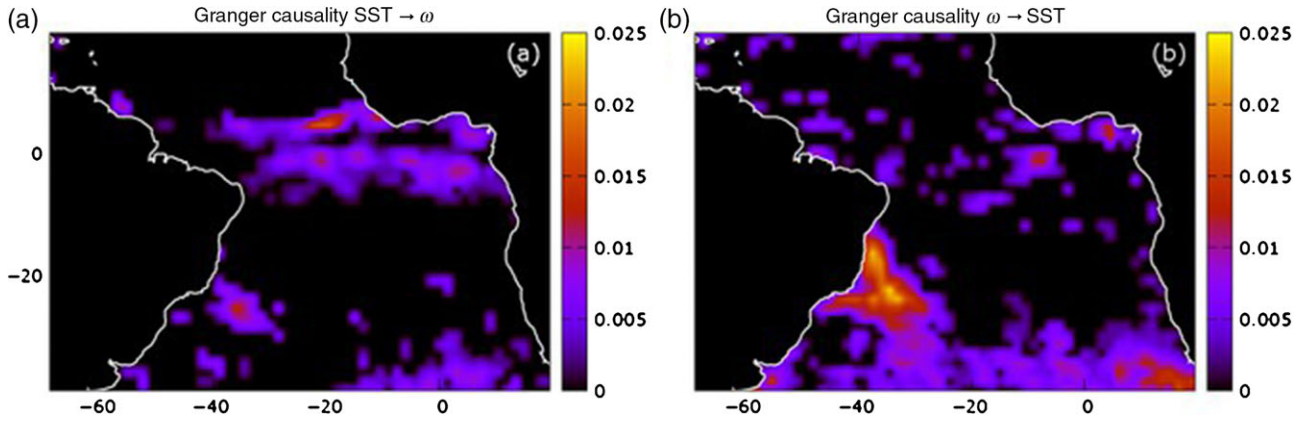
Figure 1. Local GCE for SST → ω (a) and ω → SST (b). Only values significant at 99% confidence level are reported.

ocean–atmosphere nodes. In this way, we are investigating also the presence of non-local forcing.

To represent this result, we built a two-layer network (Tsonis and Roebber, 2004) based on significant GCEs: every node of the network is a grid point of the oceanic or of the atmospheric layer, and it is linked to points in the other layer only if their GCE is significant at 99% confidence level. The resulting network is a bipartite one, i.e. a network composed of two set of nodes in which there are links only from one set to the other. Furthermore, those links are directed and allow for feedback loops.

An easy way to represent such a network is through the so-called *adjacency matrix*, **A**. The dimension of **A** is $N \times N$, where N is the number of grid points for each layer, and it is composed of only 0s and 1s. Namely, if two nodes i and j are connected, then $A_{i \rightarrow j} = 1$ and it is 0 otherwise. As the GCE is a directional measure, **A** is a non-symmetric matrix, i.e. $A_{i \rightarrow j}$ may be different from $A_{j \rightarrow i}$. For example, a location i in the ocean can be forcing a point j in the atmosphere without being forced by j itself.

Using the adjacency matrix, we can compute the AWC for the oceanic and the atmospheric layers. The AWC is defined as follows (Tsonis and Roebber, 2004):

$$\text{AWC}_i = \frac{\sum\limits_{j=1}^{N} A_{i \rightarrow j} \cos\left(\lambda_j\right)}{\sum\limits_{j=1}^{N} \cos\left(\lambda_j\right)} \qquad (4)$$

where i corresponds to the nodes in one layer, j to the nodes in the other layer, λ_j is the latitude of node j and N is the number of grid points in the studied region. The links were weighted with $\cos(\lambda_i)$ to correct the bias induced by the different areas represented by the different grid points, as it is usually done in climate network analysis (Donges *et al.*, 2009; Deza *et al.*, 2013; Tirabassi and Masoller, 2013).

It is easy to see that the AWC_i is the fraction of the region under study to which a node i is connected to. Thus, nodes with high AWC correspond to points of one layer that exercise a broad forcing on the other layer, and this way, the AWC reveals to be a powerful way to quantify

the spatial ranges of interaction of the two systems. In particular, high values of AWC indicate points that have a significant GC with many other points in the other layer. However, the AWC does not provide information about the actual value of this GC. A very weak forcing but acting over a large area, in fact, has a high value of AWC but a very low value of local GCE, while a strong forcing acting over a very narrow area has a low AWC together with a high local value of GCE. Note, however, that the AWC depends on the chosen region because atmospheric long-range teleconnections, that extend beyond the region considered, are not taken into account.

The AWC maps are depicted in Figure 2. The AWC map associated with SST → ω forcing (Figure 2(a)) presents two maxima. The first one is on the equator, at about 20W and is coincident with the tropical component of the map of local GCE. However, the largest AWC is placed offshore the southern Brazil coast and corresponds to the second maximum in the map of local GCE (Figure 1(a)). Thus, the relative magnitude of the signal in the equatorial and subtropical regions is opposed with respect to the local measure, suggesting that the SST forcing in the tropics is stronger but mainly local (vertical), while in the SACZ region it is weaker but non-local. In fact, while in the deep tropical Atlantic we have small values of AWC and high values of local GCE, in the subtropical part of the ocean the situation is the opposite, with many points presenting high AWC but relatively low values of GCE (low, compared with the tropical ones). This might be related to the fact that SST anomalies in the subtropics vary coherently on a larger spatial scale than in the equatorial Atlantic. We remark that the GCE values used to build these maps are statistically significant at 99% confidence level.

Regarding the AWC map of ω → SST (Figure 2(b)), the connectivity is generally large over the whole region, stressing the dominant role of atmospheric circulation in forcing SST anomalies. Moreover, there is a large highly connected region south of 30S, which corresponds to a largely non-local pattern of connectivity (we can see a very feeble signal in the local map in Figure 1(b)). The location of the maximum suggests that it could be related to the influence of the south Atlantic anticyclone on SST
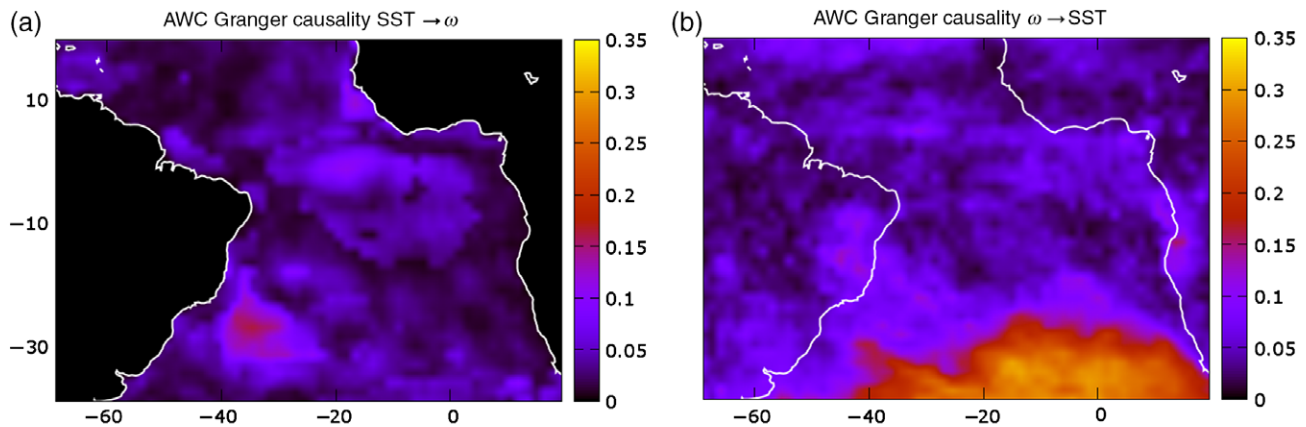
Figure 2. AWC for GC-based bilayer climate network composed of SST and ω data sets. (a) AWC computed with SST $\to \omega$ GCE. (b) AWC computed via $\omega \to$ SST GCE. Only GCE values significant at 99% confidence level have been used to compute the AWC.

through, for example, wind-induced changes in latent heat fluxes.

Taken together, these maps reveal that the SACZ region displays complex air–sea interactions in agreement with previous studies, e.g. Carvalho *et al.* (2004) and De Almeida *et al.* (2007). Nonetheless, it is important to note that the AWC maps provide information only about the spatial range of the interactions but not about their strengths. Moreover, the ω field is very noisy including several types of phenomena that need not be directly related to the SACZ dynamics. Thus, in order to gain more insight about air–sea interactions in the region, the next section focuses on the leading mode of coupled variability.

5. Directionality of air–sea coupling

The leading mode of covariability between SST and ω was computed using MCA (Bretherton *et al.* (1992)). It explains 8% of the cross covariance and is depicted in Figure 3, left column. It represents the intensification and northward shifting of the SACZ pattern with respect to the climatology, accompanied by a cooling of the SST in between the two lobes of the dipole, with maximum cooling below increased convection. As mentioned in Section 1, this dipole pattern has been shown to be the leading mode of variability in the region on several time scales (Bombardi *et al.*, 2013). Note that the region of ocean cooling is consistent with the one displayed in the AWC and in local GCE maps in Figures 1 and 2. Moreover, the map of points connected to the region of maximum AWC off Brazil reveals a structure consisting in two parallel bands oriented NW–SE, very similar in shape to Figure 3 (not shown). This suggests that this mode represents a bi-directional interaction of the two fields.

Focusing on the dynamics of the first mode, which represents the SACZ variability, allows to filter a good fraction of the weather noise and to truly concentrate on the interannual variability of the SACZ. In particular, SACZ events will evolve differently depending on the air–sea interaction.

To find the direction of the coupling between the oceanic and atmospheric patterns in the leading mode, shown in Figure 3, we calculated the GCE using the corresponding principal components (PCs) over the whole period of study. The similarity of the values obtained (0.019 in the SST $\to \omega$ direction and 0.021 in the $\omega \to$ SST one, with a relative difference of less than 10%) indicates that the air–sea interaction is very important in this mode, and confirms the results of the previous analysis, once again showing the presence of feedbacks between the atmosphere and the subtropical south Atlantic. We stress that both these values are significant at the 99% confidence level.

The second mode of covariability (7%), instead, shows the imprint of the south Atlantic anticyclone, especially in the SST component, suggesting that this is likely an atmospheric driven mode (not shown). This hypothesis was confirmed by the calculation of the GCE of the corresponding PCs (0.021 and 0.027, respectively), and the mode is not studied further here.

We next calculated the GCE for every year of the PCs (Figure 4), which allowed to classify individual years into four regimes: ω forcing SST (9 years) and SST forcing ω (4 years) if only one GCE is statistically significant, double forcing (4 years) if both GCE values are significant and neutral (17 years) if no GCE value is significant at 90% confidence level. The patterns associated with the SST forcing and neutral cases are shown in Figure 3. In the neutral case, SST anomalies are small and rainfall anomalies are strongest over land. In the SST forced case, on the contrary, there are large SST anomalies with a dipolar structure and rainfall anomalies are largest over the oceanic portion of the SACZ. Section 6 will study the evolution of these events.

From the analysis, it remains unclear whether the high number of neutral years is a consequence of the small number of data that compose the annual data sets (4 months, i.e. 121 days), or indeed, there are no significant interactions between the atmosphere and ocean. The composite analysis presented below suggests the latter.

Considering that El Niño can significantly affect the SACZ region (Barreiro *et al.*, 2002; Kayano *et al.*, 2013),
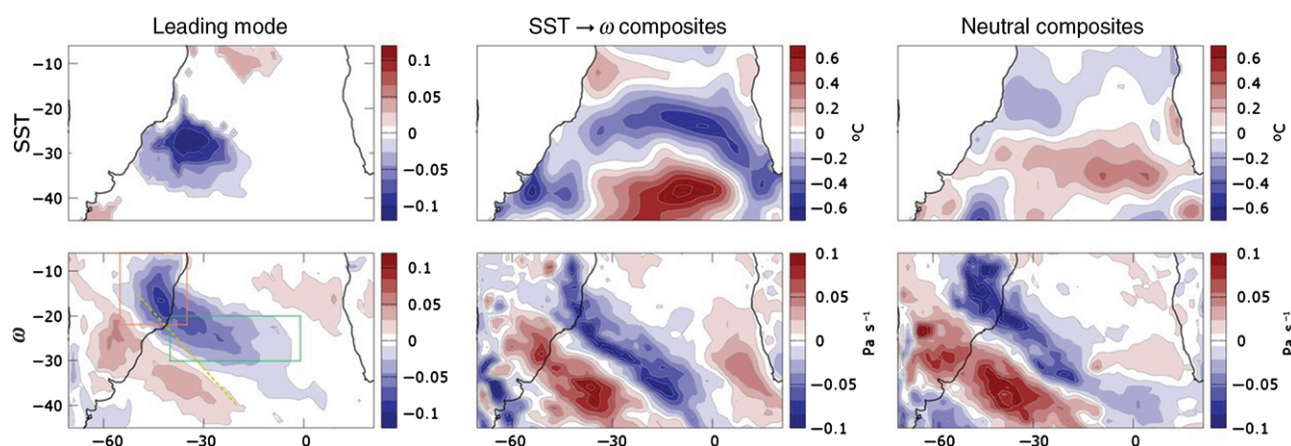
Figure 3. (Left column) Leading mode of coupled variability related to the ω and SST fields. Only significant values at 95% are reported. The dashed line represents the climatological mean position of the SACZ. (Central column) Composites for convective maxima of oceanic forcing years (SST$\rightarrow\omega$ regime, see Section 5 for details). (Right column) Composites for convective maxima of years without significant air–ocean coupling (neutral regime, see Section 5 for details). In the bottom left panel, the two boxes used for Figures 11 are depicted.
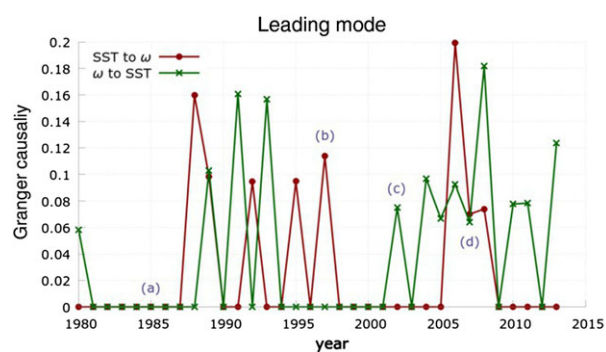

Figure 4. GCE between ω and SST PCs, relative to the leading mode of covariability. Non-significant (at 90%) GCE values are set to 0. (a) Example of years displaying of non-significant coupling, i.e. none of the two GCE values is significant. (b) Example of a year of oceanic forcing; only the SST to ω GCE value is significant. (c) Example of a year of atmospheric forcing; just the ω to SST value is significant. (d) A year of mutual forcing; both the values are significant.

Table 1. Division of the various years composing the database, respecting to the GC and ENSO classification.

	El Niño	La Niña	Neutral	Total
Neutral	4 ($p = 0.62$)	8 ($p = 0.19$)	5 ($p = 0.8$)	17
SST$\rightarrow\omega$	3 ($p = 0.10$)	0	1	4
$\omega\rightarrow$ SST	2	1	6 ($p = 0.08$)	9
SST$\leftrightarrow\omega$	1	3 ($p = 0.16$)	0	4

Some p-values are reported. The p-values are computed using a binomial distribution, taking into account both the cardinality of ENSO and PC1 classification sets.

6. Evolution of events

To study the evolution of the events in each of the four categories defined before, we constructed composites using the PC of ω corresponding to the leading mode. Thus, by construction all cases present a dipole in the vertical velocity field in the SACZ region, but the evolution of anomalies will be different. To smooth out the fields, the MCA is performed after a running-mean filtering over 3 days. The composites are calculated as the difference between the average of the 5 days presenting the largest positive peaks in the ω PC, and the average of the 5 days presenting the largest negative peaks taken from the subset of years corresponding to each category. We then repeated this computation for $[-4:4]$ days preceding and following the day of the maximum value. The composites for the four cases (Figures 5–9) are constructed for ω, SST, net surface heat fluxes, 850 hPa winds and geopotential height at 200 hPa.

6.1. Case $\omega\rightarrow$ SST

Composites of the ω field (Figure 5, last row) clearly show that the dipole starts developing at time -4 days and has almost disappeared at time $+4$ days (Figure 5, last row). In upper levels, the development of the dipole is accompanied by a travelling wave train from the extratropical Pacific sector that bends into the SACZ region as the geopotential composites show (Figure 5, second row). The lower level wind anomalies are consistent with this wave
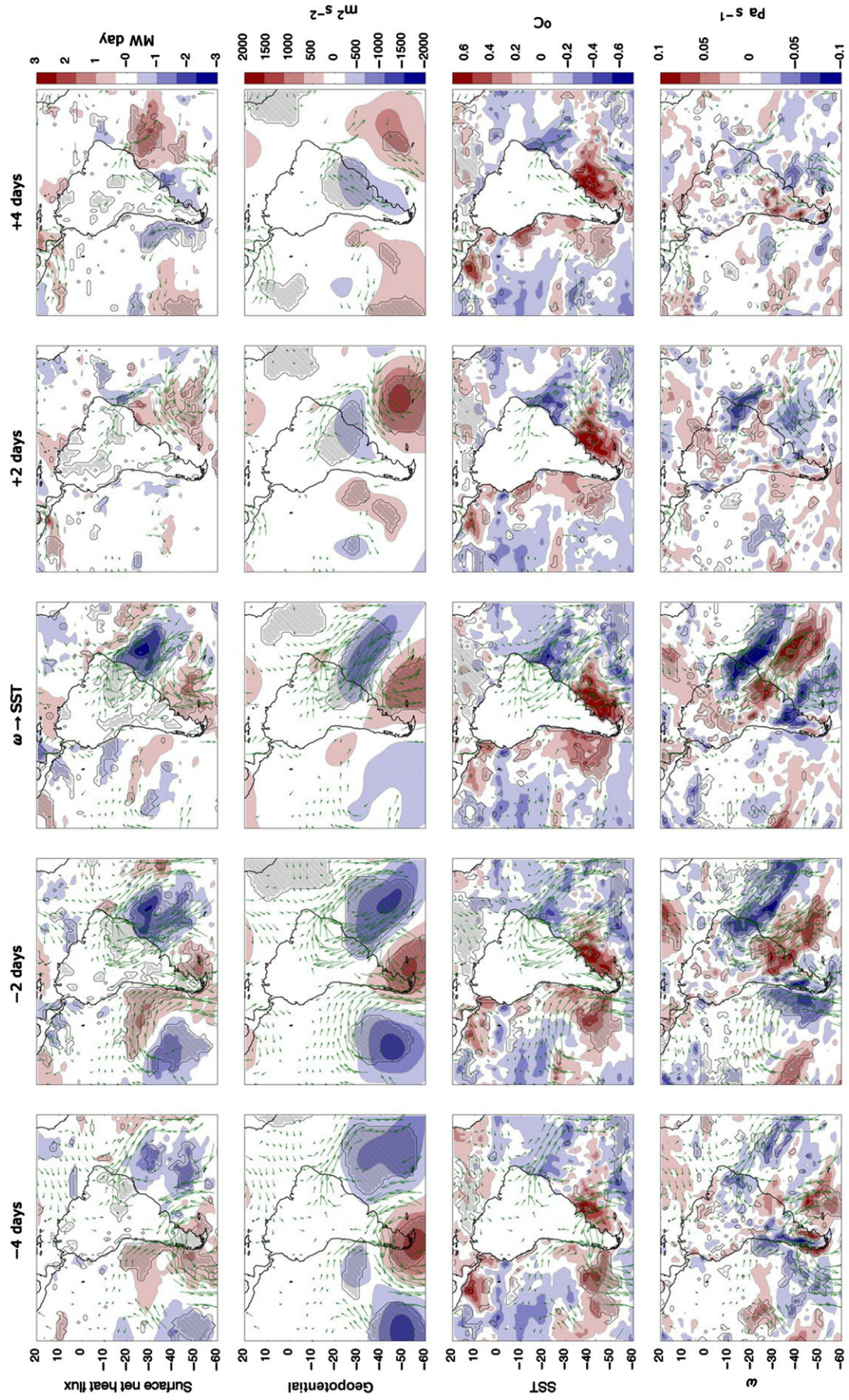
we tried to relate the occurrences of the four different regimes with the occurrence of El Niño as characterized by the NINO3.4 index. Separating the whole period in El Niño, La Niña and neutral years – according to the Oceanic Niño Index (ONI) computed with NOAA ERSSTv3b data – we can observe that the only significant combination ($p < 0.1$) is between neutral years and pure atmospheric forcing (see Table 1). In the table, the p-values are computed using a binomial distribution, taking into account both the cardinality of ENSO and PC1 classification sets. Thus, the analysis suggests that the circulation anomalies induced by El Niño and La Niña modify the regional dynamics such that the number of events of pure atmospheric forcing in the SACZ region decreases. At the same time, most of the years in which the SST forcing plays a role in the dynamics of the events (cases SST$\rightarrow\omega$ and SST$\leftrightarrow\omega$) correspond to either El Niño or La Niña years (six out of eight cases). This is discussed further in Section 6.

Figure 5. Lagged composites of ω anomalies at 500 hPa, SST anomalies, geopotential anomalies at 200 hPa and surface net heat flux anomalies for ω → SST cases. Wind anomalies at 850 hPa are also included as vector field in all the maps. Black shading marks areas of 90% significance, moreover only arrows related to wind anomalies significant at 90% are reported.
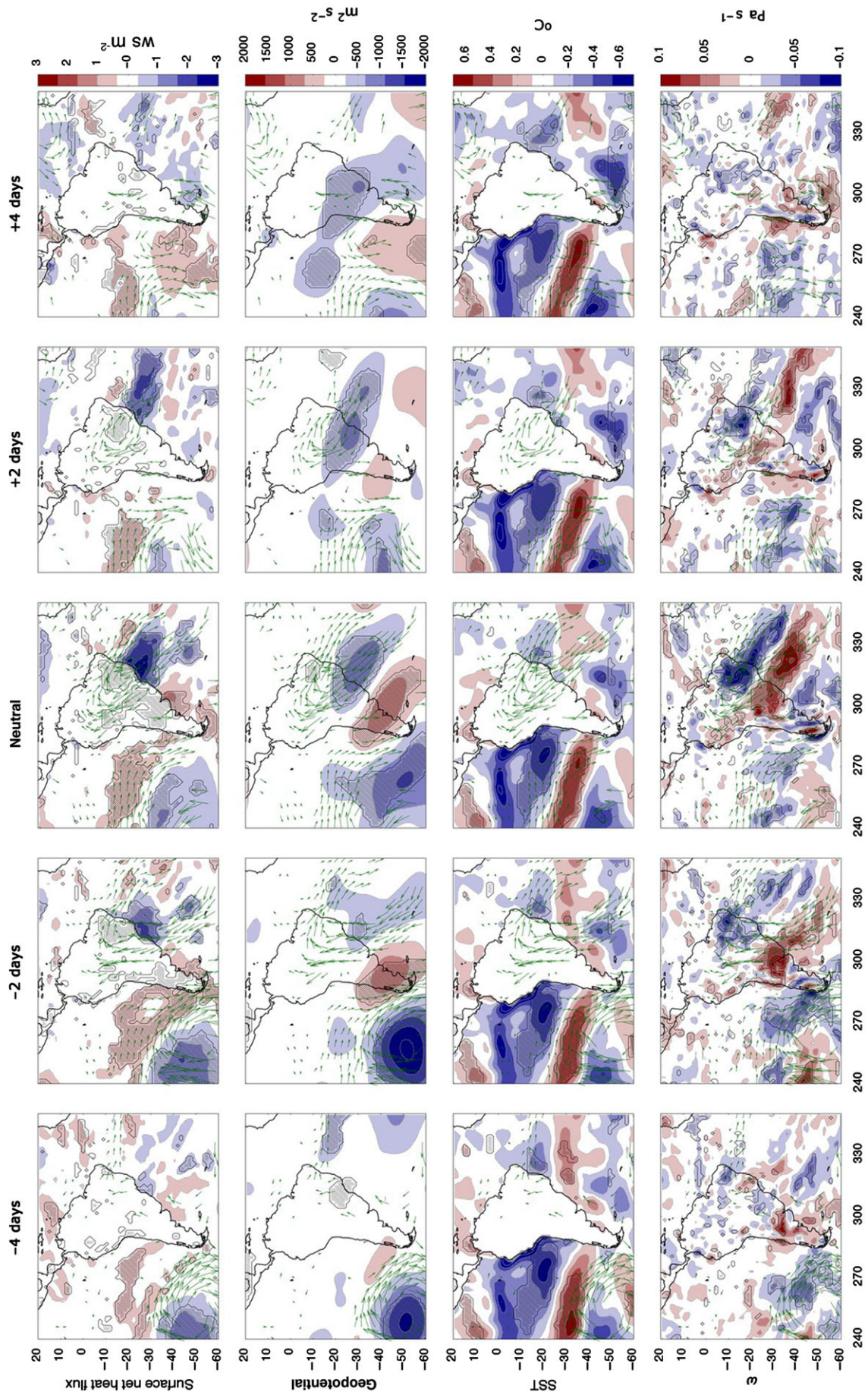
Figure 6. Lagged composites of ω anomalies at 500 hPa, SST anomalies, geopotential anomalies at 200 hPa and surface net heat flux anomalies for neutral case. Wind anomalies at 850 hPa and surface net heat flux anomalies at 200 hPa are also included as vector field in all the maps. Black shading marks areas of 90% significance, moreover only arrows related to wind anomalies significant at 90% are reported.
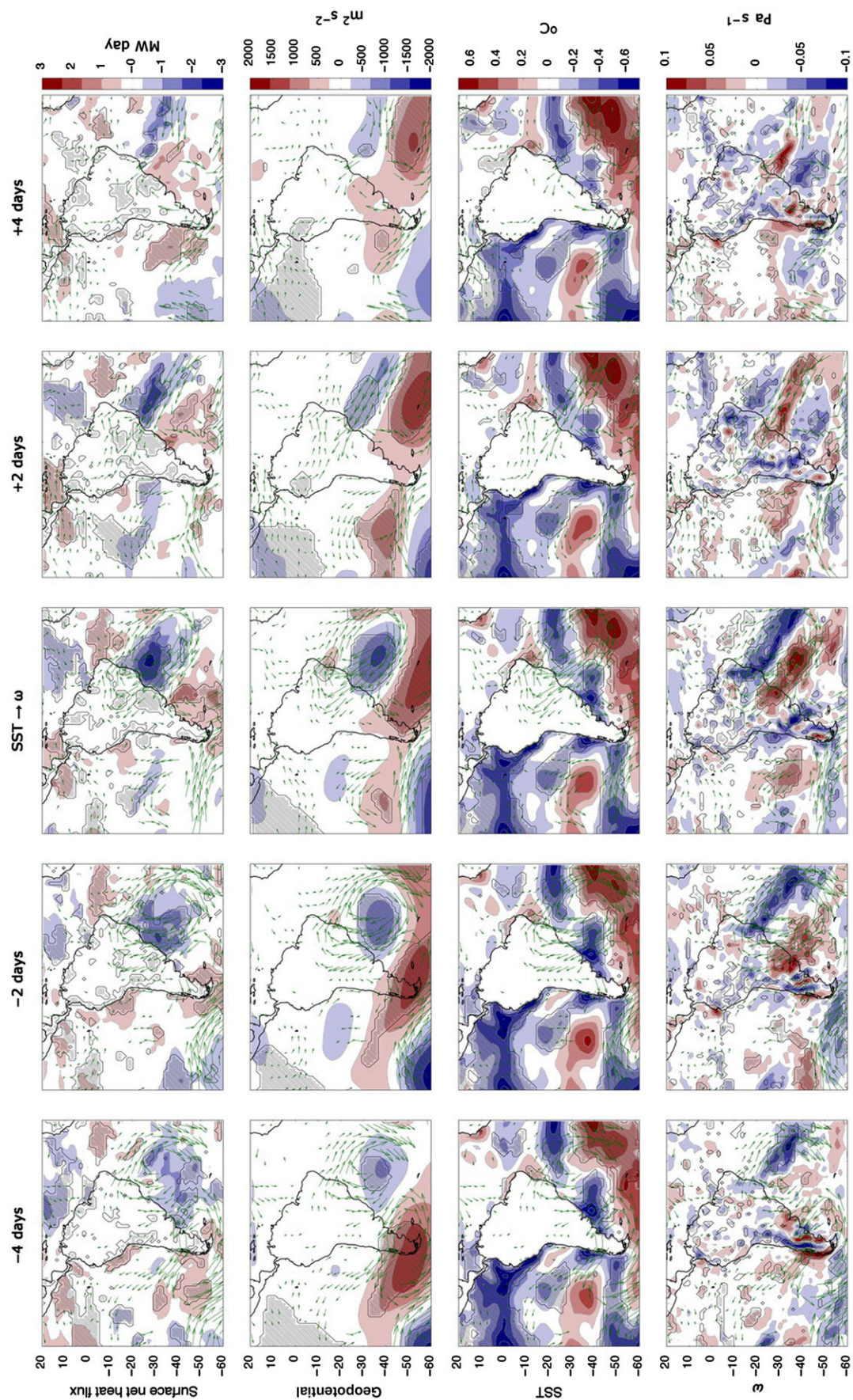
Figure 7. Lagged composites of ω anomalies at 500 hPa, SST anomalies, geopotential anomalies at 200 hPa and surface net heat flux anomalies for SST $\rightarrow \omega$ case. Wind anomalies at 850 hPa are also included as vector field in all the maps. Black shading marks areas of 90% significance, moreover only arrows related to wind anomalies significant at 90% are reported.
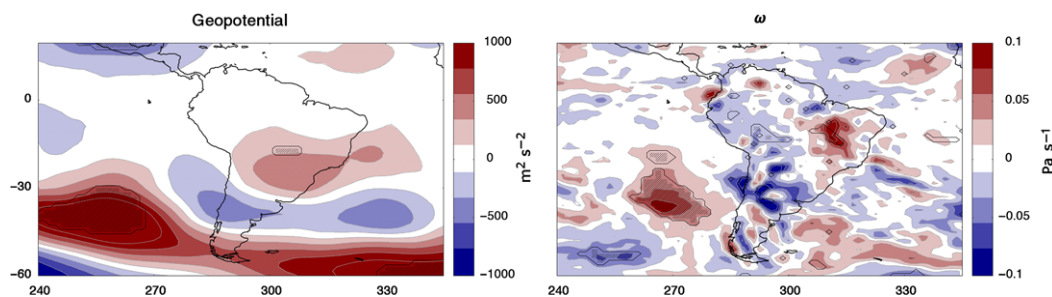
Figure 8. Differences among the lag-0 composite maps of the two cases SST → ω and neutral. (a) Differences between the maps of geopotential anomalies at 200 hPa composites. (b) Differences between the maps of ω anomalies at 500 hPa composites. Black shading marks areas of 90% significance.

train, and there is clear cyclonic circulation in the SACZ that generates convergence (divergence) in the region of upward (downward) motion. This behaviour is consistent with the literature that suggests that mid-latitude Rossby wave trains modulate the activity of the SACZ on time scales of a few days, such that intensified SACZ events are accompanied by upper level troughs to the southwest (Kiladis and Weickmann, 1997; Cavalcanti and Kayano, 1999; Liebmann *et al.*, 1999; Carvalho *et al.*, 2004). The atmospheric forcing is clearly seen in the maps of net surface heat flux, which show large heat losses from day −4 to the peak cooling the SST below next to the Brazilian coast (Figure 5, first row). Regions with southeasterlies induce strong latent and sensible heat flux loses between [55W–30W, 30S–50S] up to day 0; after the peak, the latent and sensible heat flux anomalies change sign (not shown). The pattern of shortwave and longwave radiative fluxes follow the shape of the ω anomalies such that increased ascent decreases shortwave and increases longwave fluxes at the surface through enhanced cloudiness (not shown). Note that after the peak, the net surface heat flux changes sign such that at day +4 the ocean is gaining a significant amount of heat that weakens the created SST anomaly off southeast Brazil (Figure 5, third row). The net heat flux anomaly is dominated by the latent heat because the oceanic extension of the SACZ weakens rapidly after the peak.

6.2. Case neutral

The evolution of atmospheric anomalies in this case is similar to the previous one, and it is reported in Figure 6. In the geopotential composites, there is an upper level wave train that progresses from the extratropical Pacific and bends into South America. However, the path of the wave in this latter case is more meridionally oriented so that the centre of the cyclonic anomaly in the SACZ region is closer to the coast allowing surface level winds to penetrate further into the continent. For example, at the peak there are southerly winds up to the Equator, while in the ω → SST case the southerly winds reach only to 10S. As a consequence, the low-level wind anomalies are able to transport moisture more effectively from the Amazon basin towards the northern sector of the SACZ. This results in ω anomalies that have largest values over the

continent and weaker over the oceanic portion of the SACZ (Figure 6, last row). Surface heat fluxes are also negative below the SACZ, although they are weaker than in the previous case, and cool the SST off Brazil (Figure 6, first and third rows). However, in this case the net surface heat flux does not change sign after the peak below the SACZ. The negative heat fluxes below the enhanced portion of the SACZ are primarily due to decreased shortwave radiation and increased latent heat flux (Figure 10). The oceanic loss of latent heat below an enhanced SACZ provides more moisture for rainfall and thus supports the maintenance of the oceanic extension of the SACZ. Moreover, the surface wind anomalies after the peak keep blowing from the ocean to the continent providing enhanced moisture supply. Thus, in this case the persistence of the oceanic portion of the SACZ is larger than in the ω → SST case (see also Figure 10). Therefore, in the neutral case there seems to exist two-way air–sea interaction. However, as the largest anomalies occur over land, this process does not significantly impact the evolution of the event and thus this category does not show any significant air–sea interaction according to the GC measure. It would be very interesting to study the land–atmosphere interaction in this category.

6.3. Case SST → ω

As shown in Table 1, most of these cases occur during El Niño years. According to the literature, El Niño induces positive upper level geopotential height anomalies over tropical South America and positive sea level pressure anomalies in the tropical Atlantic during this season (e.g. Alexander and Scott (2002)). In addition, El Niño forces extratropical wave trains that propagate from the Pacific towards South America in arch-like paths, a mechanism that weakens during summertime – for a review, see Grimm and Ambrizzi (2009). In the events of this category, we see mainly evidence for an influence of the tropical Pacific via extratropical wave forcing (Figure 7, second row). We found that cases with decreased rainfall in the northern side of the SACZ dipole correspond to El Niño, thus the SST composite constructed here shows negative anomalies in the eastern Pacific (Figure 7, third row). The composite of the geopotential height at 200 hPa shows evidence of a wave train coming from the extratropical Pacific with negative and positive centres south of 50S that arches
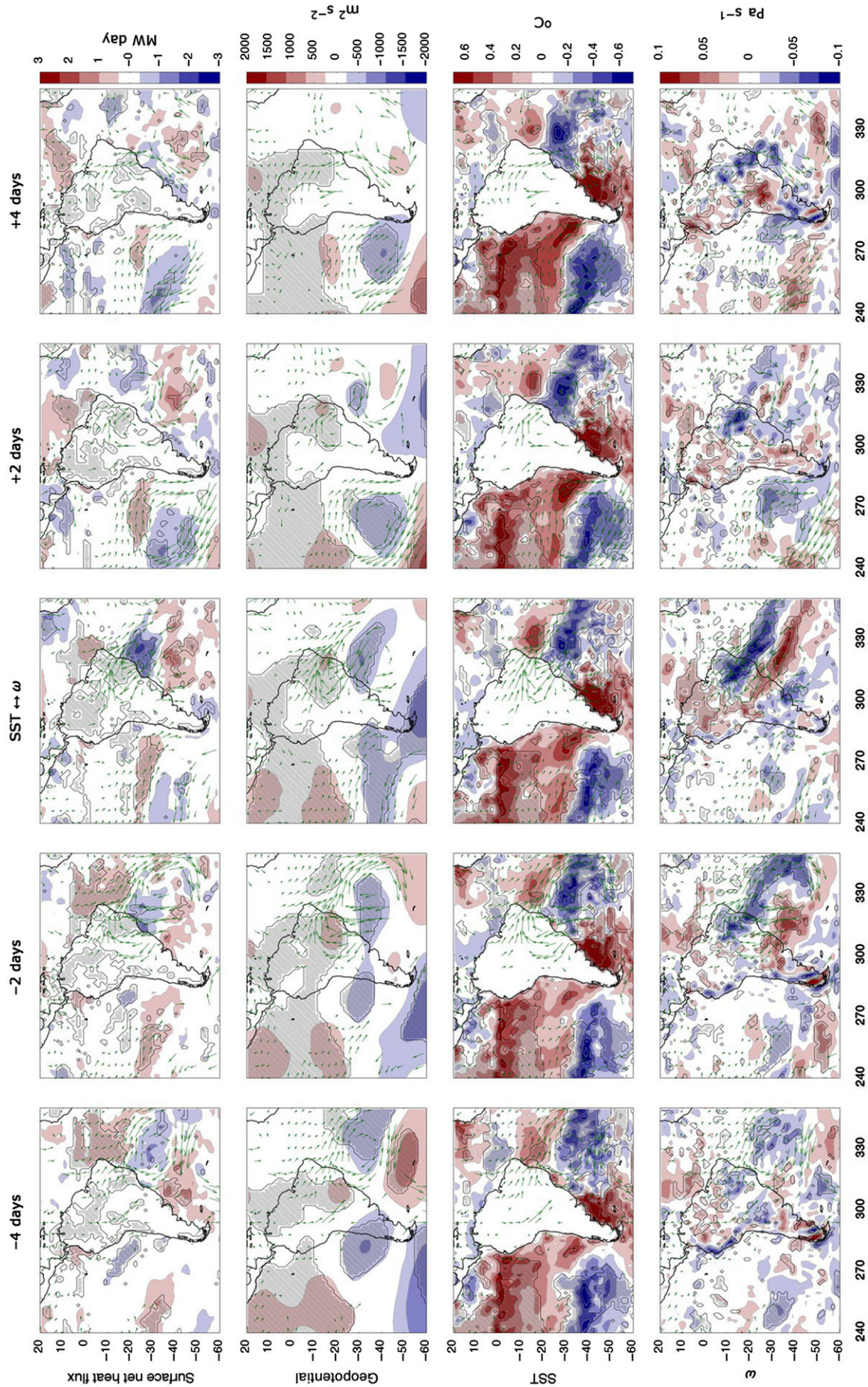
Figure 9. Lagged composites of ω anomalies at 500 hPa, SST anomalies, geopotential anomalies at 200 hPa and surface net heat flux anomalies for SST ↔ ω case. Wind anomalies at 850 hPa are also included as vector field in all the maps. Black shading marks areas of 90% significance, moreover only arrows related to wind anomalies significant at 90% are reported.
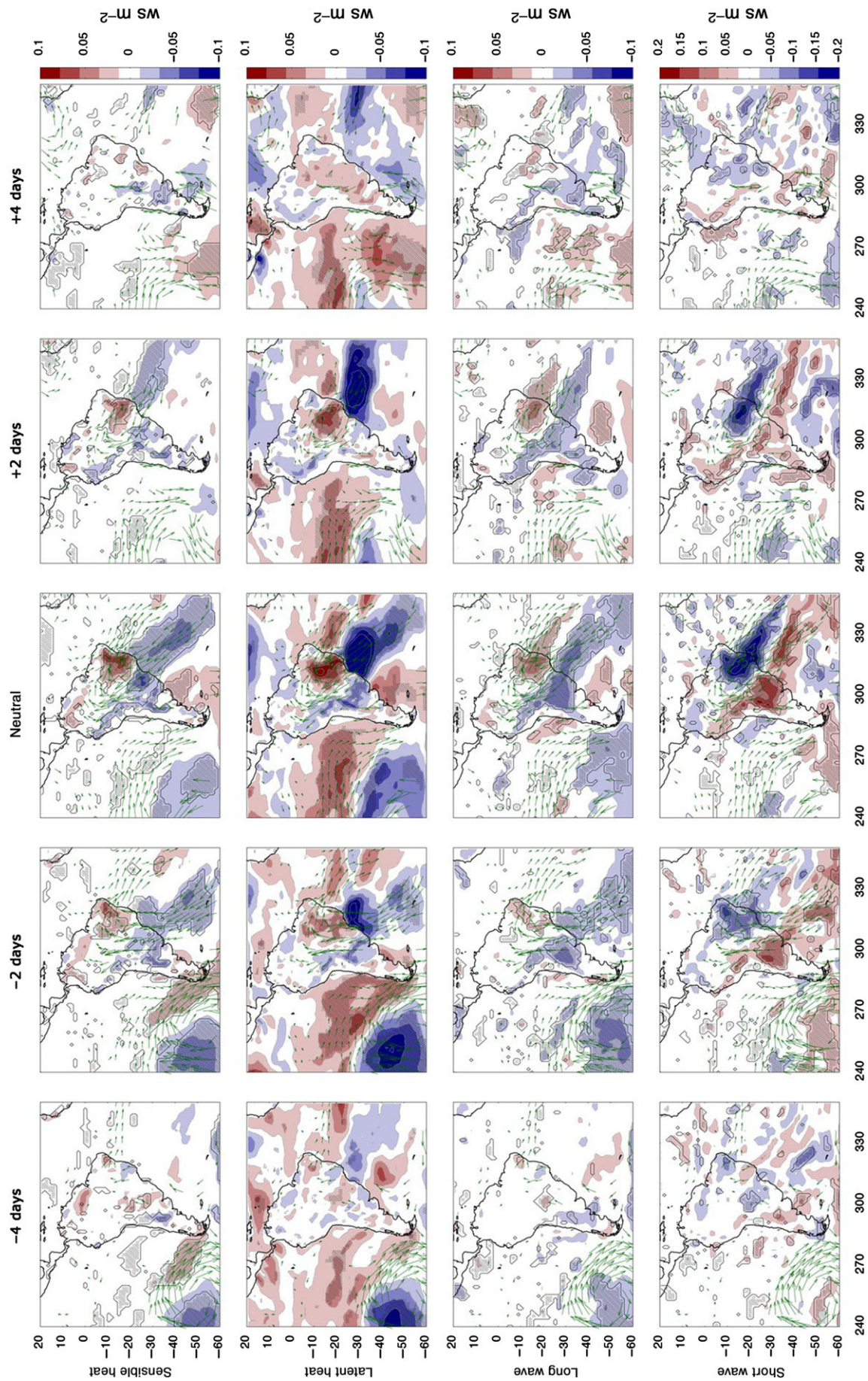
Figure 10. Composites of surface heat components and wind anomalies, at 850 hPa for the neutral case. Black shading marks areas of 90% significance, only arrows related to wind anomalies significant at 90% are reported.

towards the tropical Atlantic to the east of South America. This wave train has a stationary component as the centres of the anomalies move slowly from day −4 to day +4 (Figure 7, second row). In addition to the wave train, there is a positive geopotential height anomaly centred at (40S, 90W) that persist during the whole event. This is in clear contrast to the previous two cases (e.g. $\omega \to$ SST and neutral, Figures 5 and 6) and indicates the influence of the tropical Pacific forcing. Superposed on the stationary wave component, there is a travelling wave train that shifts the pattern westward and intensifies the atmospheric anomalies. The resulting path of the wave is quite south and the surface wind anomalies in the SACZ region are located mainly over the ocean. Thus, the ω anomalies in Figure 7 are strongest in the oceanic portion of the SACZ with only weak continental extension. Moreover, the oceanic dipole of ω anomalies persists up to day +4, albeit weakening with time.

To further illustrate the distinct behaviour of this case with respect to the previous one, in Figure 8 we report the difference in atmospheric circulation anomalies between SST $\to \omega$ and neutral cases at the peak of the event. Consistent with the previous description, the geopotential difference shows a ridge over the continent and a trough over the ocean indicating that the negative geopotential anomalies in the SST $\to \omega$ are shifted over the ocean. Furthermore, due to its barotropic structure the ridge over eastern Brazil is associated with increased northerlies into the subtropics and easterlies in northeast Brazil. This induces moisture flux anomalies and the continental convection dipole observed in Figure 8(b), which indicates smaller continental rainfall anomalies in the SST $\to \omega$ compared with the neutral case. In higher latitudes, there are large differences in the geopotential field reflecting differences in the behaviour of the wave associated with the two cases and mentioned before.

On the oceanic side, the Atlantic SST anomaly field is dominated by a strong dipole with cold anomalies north of 30S and warm anomalies to the south, except to the south of Uruguay. This SST pattern is conspicuous during summertime and is related to a strengthening of the south Atlantic anticyclone on seasonal time scales (Barreiro *et al.*, 2004). As in the previous cases, there is strong heat loss off Brazil from day −4 to the peak, which cools the SST below. The southeasterly component of the surface winds provide more moisture to the region of enhanced ascent. Moreover, in the days following the peak, there is oceanic latent heat loss below the region of anomalous ascent which, as in the Neutral case, implies anomalous moisture flux into the atmosphere that helps maintaining the ω (rainfall) anomalies over the oceanic portion of the SACZ up to day +4 (Figures 6 and 7). In this case, as most of the atmospheric anomalies are located over the ocean, the evolution of the rainfall dipole is influenced by the SST. These results suggest that of central importance for the SST to influence the evolution of SACZ events is that atmospheric anomalies have to be located mainly over the ocean. According to our results, this means that the extratropical wave trains have to propagate mainly zonally

and bend only slightly into the tropical Atlantic. Since 3 out of 4 years in this category correspond to El Niño years, it suggests that changes in the mean state caused by a warming in the equatorial Pacific may change the propagation properties of the wave trains through changes in the jet streams or blocking as found during winter by Oliveira *et al.* (2014). More research is needed to fully address this issue , including understanding what is special about these three El Niño events.

6.4. Case SST $\leftrightarrow \omega$

According to Table 1, most of these cases occur during La Niña years and correspond to years with dipole events that have negative rainfall anomalies in the northern portion of the SACZ (Figure 9). Contrary to the case SST $\to \omega$, here the tropical anomalies induced by the equatorial Pacific Ocean are more significant than the extratropical wave forcing (compare composites for the geopotential height in 200 hPa and for the surface winds in Figures 7 and 9). As consequence, there are northwesterly surface wind anomalies in northeastern Brazil that last the whole event and help the development of convergence there (Figure 9, second row). In addition, over the continental SACZ region, there is a positive geopotential height anomaly that, due to its baroclinic nature, has a low pressure associated at the surface that seems to play an important role in the event. Together with the low-pressure centre associated with a weak extratropical wave train, they generate the cyclonic wind anomaly associated with the peak rainfall dipole in the SACZ. Note that at day −4 the convective anomalies over land and over the ocean develop separately and merge at day −2 when the surface low-pressure centre over the ocean moves westward. The travelling wave train in the geopotential composites is the weakest of all four categories having the maximum at day −4. At the peak, the surface wind anomalies and oceanic heat loss are relatively weak (Figure 9, first row). At day +2, there is a dipole in surface net heat flux anomalies with similar structure but weaker in magnitude than the one in SST $\to \omega$ case, but at day +4 heat fluxes are no longer significant. Finally, the region of ascent motion over the continent lasts from day −4 to day +4, the longest of all categories, probably due to the favourable conditions maintained by El Niño (Figure 9, last row). As anomalies are relatively weak and El Niño seems to play an important role, it is hard to pinpoint how the ocean and atmosphere interact and more work is needed to understand this case. One possibility would be to repeat the Granger analysis after removing El Niño influence, but that is beyond the scope of this study.

As an additional analysis to compare the four regimes, we report in Figure 11 the time evolution of ω anomaly in the composites computed in two different boxes: one in the continental box [22S; 6S] $\times$ [55W; 35W], and another in an oceanic box at [40S; 30S] $\times$ [40W; 1W]. The two boxes, depicted in Figure 3, were chosen to characterize the strength of the anomalies over the continent and the oceanic extension of the SACZ. The lag times in Figure 11
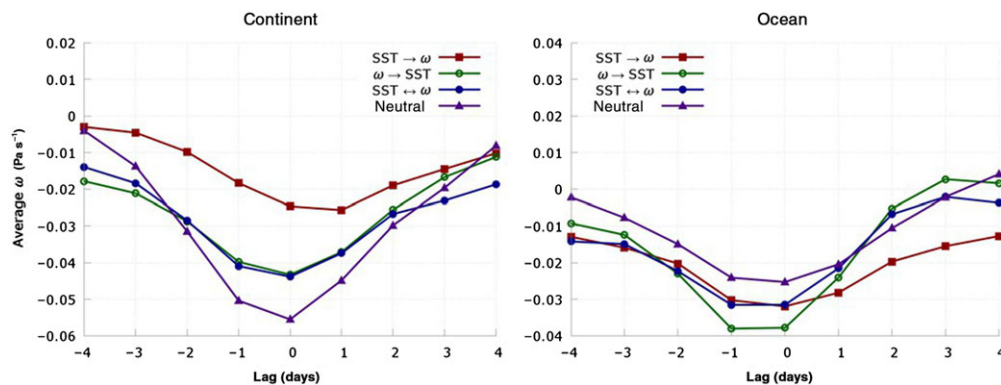
Figure 11. Composites of average ω anomalies in Continental ([22S;6S]$\times$[55W;35W] (a) and Oceanic ([40S;30S]$\times$[40W,1W] (b) boxes (see text for details).

are the same of Figures 5–7 and 9, thus the 0 lag corresponds to the convective peak. It can be seen that the overall evolution of anomalies over the continental region are quite symmetric about day 0, except in the case of ocean forcing. In this latter case, the peak occurs at day +1 and anomalies tend to persist. Over the oceanic region, anomalies are generally smaller in magnitude and have similar values at day −1 and day 0. The neutral case is the one characterized by weakest positive precipitation anomalies over the ocean and largest over the continent. The SST $\rightarrow \omega$ case, on the other hand, shows weakest rainfall anomalies over the continent, but has largest persistence of anomalies over the ocean. Cases $\omega \rightarrow$ SST and SST $\leftrightarrow$ show a very similar evolution over the continent, except at the end of the event when cases SST $\leftrightarrow \omega$ have larger persistence. Over the ocean, case $\omega \rightarrow$ SST shows the largest anomalies, but do not persist for long: after the peak, the vertical velocity rapidly goes back to zero at day +2. This is in sharp contrast with the case SST $\rightarrow \omega$ where anomalies at day +2 are still large.

7. Summary

Air–sea interactions in the region of the SACZ are studied using the GCE as a measure of directional coupling. A first important result is that this region has a large mutual air–sea connectivity during summertime. Introducing a new method that combines GC with MCA, we have been able to identify four regimes, depending on the direction of the air–sea interaction. In particular, we identified years in which the coupling is mainly directed from the ocean to the atmosphere, years in which the coupling is from the atmosphere to the ocean, years of mutual interactions and years of no significant coupling.

We studied the evolution of the convective events related to these different regimes looking at atmospheric and surface oceanic fields and found that in all cases an extratropical wave train plays a major role in forcing convection in the SACZ, as suggested previously by several authors. Moreover, we found that the path of the wave seems to be instrumental in determining the evolution of the SACZ event. For example, if the path

of the wave bends significantly over South America, the largest anomalies develop first and are more intense over the continent, the oceanic extension of the SACZ is weak and there is no air–sea coupling (Neutral cases). On the other hand, in ocean-forced cases, the extratropical wave train is further to the south so that the strongest convective anomalies develop over the oceanic portion of the SACZ, allowing the ocean to force atmospheric anomalies that tend to persist longer than in other regimes. We also found that these events are more frequent during El Niño years.

Further study of the SACZ using this methodology combined with tailored numerical experiments that, for example, isolate the effects of El Niño are needed to further understand the complex air–sea interactions in this region.

References

Alexander M, Scott J. 2002. The influence of ENSO on air–sea interaction in the Atlantic. *Geophys. Res. Lett.* **29**(14): 46–49.

Attanasio A, Pasini A, Triacca U. 2012. A contribution to attribution of recent global warming by out-of-sample Granger causality analysis. *Atmos. Sci. Lett.* **13**(1): 67–72.

Barreiro M, Chang P, Saravanan R. 2002. Variability of the South Atlantic Convergence Zone as simulated by an atmospheric general circulation model. *J. Clim.* **15**: 745.

Barreiro M, Giannini A, Chang P, Saravanan R. 2004. On the role of the South Atlantic atmospheric circulation in tropical Atlantic variability. In *Earth's Climate*, Wang C, Xie SP, Carton JA (eds). American Geophysical Union: Washington, DC, doi: 10.1029/147GM08.

Barreiro M, Chang P, Saravanan R. 2005. Simulated precipitation response to SST forcing and potential predictability in the region of the South Atlantic Convergence Zone. *Clim. Dyn.* **24**: 105–114.

Bombardi RJ, Carvalho LMV, Jones C, Reibota MS. 2013. Precipitation over eastern South America and the South Atlantic sea surface temperature during Neutral ENSO periods. *Clim. Dyn.* **42**: 1553–1568.

Bretherton CS, Smith C, Wallace JM. 1992. An intercomparison of methods for finding coupled patterns in climate data. *J. Clim.* **5**: 541–560.

Carvalho LMV, Jones C, Liebmann B. 2002. Extreme precipitation events in southeastern South America and large-scale convective patterns in the South Atlantic Convergence Zone. *J. Clim.* **15**: 2377–2394.

Carvalho LMV, Jones C, Liebmann B. 2004. The South Atlantic Convergence Zone: intensity, form, persistence, and relationships with intraseasonal to interannual activity and extreme rainfall. *J. Clim.* **17**: 88–107.

Cavalcanti IFA, Kayano MT. 1999. High-frequency patterns of the atmospheric circulation over the Southern Hemisphere and South America. *Meteorol. Atmos. Phys.* **69**(3–4): 179–193.

Chatfield C. 1989. *The Analysis of Time Series: An Introduction*, 4th edn. Chapman & Hall: New York, NY.

Chaves RR, Nobre P. 2004. Interactions between sea surface temperature over the South Atlantic Ocean and the South Atlantic Convergence Zone. *Geophys. Res. Lett.* **31**: L03204, doi: 10.1029/2003GL018647.

De Almeida RAF, Nobre P, Haarsma RJ, Campos EJD. 2007. Negative ocean-atmosphere feedback in the South Atlantic Convergence Zone. *Geophys. Res. Lett.* **34**(18): L18809.

Dee DP, Uppala SM, Simmons AJ, Berrisford P, Poli P, Kobayashi S, Andrae U, Balmaseda MA, Balsamo G, Bauer P, Bechtold P, Beljaars ACM, van de Berg L, Bidlot J, Bormann N, Delsol C, Dragani R, Fuentes M, Geer AJ, Haimberger L, Healy SB, Hersbach H, Hólm EV, Isaksen L, Kållberg P, Köhler M, Matricardi M, McNally AP, Monge-Sanz BM, Morcrette J-J, Park B-K, Peubey C, de Rosnay P, Tavolato C, Thépaut J-N, Vitart F. 2011. The ERA-Interim reanalysis: configuration and performance of the data assimilation system. *Q. J. R. Meteorol. Soc.* **137**: 553–597.

Deza JI, Barreiro M, Masoller C. 2013. Inferring interdependencies in climate networks constructed at inter-annual, intra-season and longer time scales. *Eur. Phys. J. Spec. Top.* **222**(2): 511–523.

Donges JF, Zou Y, Marwan N, Kurths J. 2009. The backbone of the climate network. *EPL* **87**: 4.

Grimm AM, Ambrizzi T. 2009. Teleconnections into South America from the tropics and extratropics on interannual and intraseasonal timescales. In *Past Climate Variability in South America and Surrounding Regions*. Springer: London, 159–191.

Hoskins BJ, Karoly DJ. 1981. The steady linear response of a spherical atmosphere to thermal and orographic forcing. *J. Atmos. Sci.* **38**: 61179–61196.

Junquas C, Vera C, Li L, Le Treut H. 2012. Summer precipitation variability over Southeastern South America in a global warming scenario. *Clim. Dyn.* **38**(9–10): 1867–1883.

Kayano MT, Andreoli RV, Ferreira de Souza RA. 2013. Relations between ENSO and the South Atlantic SST modes and their effects on the South American rainfall. *Int. J. Climatol.* **33**: 2008–2023, doi: 10.1002/joc.3569.

Khokhlov VN, Glushkov AV, Loboda NS. 2006. On the nonlinear interaction between global teleconnection patterns. *Q. J. R. Meteorol. Soc.* **132**(615): 447–465.

Kiladis GN, Weickmann KM. 1997. Horizontal structure and seasonality of large-scale circulations associated with submonthly tropical convection. *Mon. Weather Rev.* **125**(9): 1997–2013.

Kodama YM. 1992. Large-scale common features of subtropical precipitation zones (the Baiu frontal zone, the SPCZ, and the SACZ). Part I: characteristics of subtropical frontal zones. *J. Meteorol. Soc. Jpn.* **70**: 813–836.

Liebmann B, Kiladis GN, Marengo JA, Ambrizzi T, Glick JD. 1999. Submonthly convective variability over South America and the South Atlantic Convergence Zone. *J. Clim.* **12**(7): 1877–1891.

Mokhov II, Smirnov DA, Nakonechny PI, Kozlenko SS, Seleznev EP, Kurths J. 2011. Alternating mutual influence of El-Niño/Southern Oscillation and Indian monsoon. *Geophys. Res. Lett.* **38**: L00F04.

Mosedale TJ, Stephenson DB, Collins M, Mills TC. 2006. Granger causality of coupled climate processes: ocean feedback on the North Atlantic Oscillation. *J. Clim.* **19**: 1182.

Nogués-Paegle J, Mo KC. 1997. Alternating wet and dry conditions over South America during summer. *Mon. Weather Rev.* **125**: 2.

Oliveira FNM, Carvalho L, Ambrizzi T. 2014. A new climatology for Southern Hemisphere blockings in the winter and the combined effect of ENSO and SAM phases. *Int. J. Climatol.* **34**(5): 1676–1692.

Pasini A, Triacca U, Attanasio A. 2012. Evidence of recent causal decoupling between solar radiation and global temperature. *Environ. Res. Lett.* **7**: 3.

Robertson AW, Mechoso CR. 2000. Interannual and interdecadal variability of the South Atlantic Convergence Zone. *Mon. Weather Rev.* **128**(8): 2947–2957.

Runge J, Petoukhov V, Kurths J. 2014. Quantifying the strength and delay of climatic interactions: the ambiguities of cross correlation and a novel measure based on graphical models. *J. Clim.* **27**(2): 720–739.

Salvucci GD, Saleem JA, Kaufmann R. 2002. Investigating soil moisture feedbacks on precipitation with tests of Granger causality. *Adv. Water Resour.* **25**(8): 1305–1312.

Schwarz G. 1978. Estimating the dimension of a model. *Ann. Stat.* **6**(2): 461–464.

Stern DI, Kaufmann RK. 1999. Econometric analysis of global climate change. *Environ. Model. Softw.* **14**(6): 597–605.

Stern DI, Kaufmann RK. 2014. Anthropogenic and natural cause of climate change. *Clim. Change* **122**(1–2): 247–269.

Tirabassi G, Masoller C. 2013. On the effects of lag-times in networks constructed from similarities of monthly fluctuations of climate fields. *EPL* **102**: 5.

Tsonis AA, Roebber PJ. 2004. The architecture of the climate network. *Phys. A* **333**: 497–504.